

# ChemComm

Chemical Communications

rsc.li/chemcomm



ISSN 1359-7345

**COMMUNICATION**

Dianming Sun, Xiao-Hong Zhang, Eli Zysman-Colman *et al.*  
A fluorene-bridged double carbonyl/amine multiresonant  
thermally activated delayed fluorescence emitter for  
efficient green OLEDs


 Cite this: *Chem. Commun.*, 2024, 60, 2489

 Received 25th November 2023,  
 Accepted 21st December 2023

DOI: 10.1039/d3cc05761e

rsc.li/chemcomm

# A fluorene-bridged double carbonyl/amine multiresonant thermally activated delayed fluorescence emitter for efficient green OLEDs†‡

 Sen Wu,<sup>§a</sup> Ya-Nan Hu,<sup>§b</sup> Dianming Sun,<sup>\*a</sup> Kai Wang,<sup>ib</sup> Xiao-Hong Zhang<sup>ib</sup> \*<sup>bc</sup> and Eli Zysman-Colman<sup>id</sup> \*<sup>a</sup>

Herein, we report a fluorene-bridged double carbonyl/amine-based MR TADF emitter DDiKTa-F, formed by locking the conformation of the previously reported compound DDiKTa. Using this strategy, DDiKTa-F exhibited narrower, brighter, and red-shifted emission. The OLEDs with DDiKTa-F emitted at 493 nm and showed an EQE<sub>max</sub> of 15.3% with an efficiency roll-off of 35% at 100 cd m<sup>-2</sup>.

Thermally activated delayed fluorescence (TADF) materials have demonstrated great potential as next-generation emitters in organic light-emitting diodes (OLEDs) due to their ability to harness 100% of the excitons to produce light without the need for noble metals, present in phosphorescent OLEDs. TADF compounds convert non-emission triplet excitons into emissive singlets by an endothermic upconversion reverse intersystem crossing (RISC) process.<sup>1–4</sup> The efficiency of the RISC process is governed in part by the singlet-triplet energy gap, ΔE<sub>ST</sub>.<sup>5</sup> A strongly twisted structure that effectively reduces the conjugation between donor and acceptor moieties is one strategy to achieve a small ΔE<sub>ST</sub> as the exchange integral of the frontier molecular orbitals (FMOs) is small.<sup>4</sup> However, a twisted structure exhibits significant excited-state structural relaxation, resulting in a broad emission characterized by a full width at half maximum (FWHM) higher than 70 nm.<sup>6</sup> To compensate for the

broad emission, filters or microcavities are required to improve color purity; however, this can, unfortunately, reduce the device efficiency.<sup>7</sup>

Multiresonant TADF (MR-TADF) emitters have emerged as a potential solution as these rigid structures exhibit narrowband emission. First reported by Hatakeyama *et al.*, these compounds are p- and n-doped polycyclic aromatic hydrocarbons (PAHs).<sup>8</sup> By employing this approach, the singlet and triplet excited states possess an alternating pattern of increasing and decreasing electron density compared to the ground state, thus enabling a small exchange integral and consequently a small ΔE<sub>ST</sub>.<sup>9</sup> The rigid structure and the short-range charge transfer (SRCT) nature of the excited states endow the MR-TADF compounds with bright, narrowband emission. Since the first report of MR-TADF emitters used in OLEDs in 2016, there has been intense research focused on expanding the chemical space encompassed by this class of emitters.<sup>10</sup> In the original works of Hatakeyama *et al.*, the n-dopants were boron atoms. It is possible to replace these with carbonyl groups, and the groups of Zysman-Colman<sup>11</sup> Zhang,<sup>12</sup> and Jiang and Liao<sup>13</sup> were among the first to report examples of MR-TADF emitters containing this motif. Expanding the MR-TADF skeleton has been demonstrated to be an effective strategy for improving the performance of MR-TADF emitters,<sup>14</sup> which has been less explored in carbonyl/amine systems.

We have shown that the dimerization of the MR-TADF emitter, DiKTa, in DDiKTa, leads to a modest red-shift of the emission and the OLED showed an improved performance.<sup>15</sup> In an attempt to further improve the device performance and reduce the structural motion inherent in DDiKTa, here, we envisioned annealing together two DiKTa units through a central 9,9-dimethyl-9H-fluorene bridge, DDiKTa-F. An analogue without the *tert*-butyl groups was also synthesized; however, purification proved too difficult owing to its poor solubility, likely due to its strong propensity to aggregate. Therefore, two *tert*-butyl groups were added to improve the solubility of this compound. DDiKTa-F was found to be brighter (photoluminescence quantum yield, Φ<sub>PL</sub>, of 78%) and emits with a narrower FWHM, of 49 nm compared to DDiKTa (Φ<sub>PL</sub> of 68% and FWHM of 59 nm) in 2 wt% doped films in 1,

<sup>a</sup> Organic Semiconductor Centre, EaStCHEM School of Chemistry, University of St Andrews, St Andrews, Fife KY16 9ST, UK.

 E-mail: eli.zysman-colman@st-andrews.ac.uk, sd235@st-andrews.ac.uk;  
 Fax: +44-1334 463808; Tel: +44-1334 463826

<sup>b</sup> Institute of Functional Nano & Soft Materials (FUNSOM), Joint International Research Laboratory of Carbon-Based Functional Materials and Devices, Soochow University, Suzhou, Jiangsu 215123, P. R. China.  
 E-mail: xiaohong\_zhang@suda.edu.cn

<sup>c</sup> Jiangsu Key Laboratory of Advanced Negative Carbon Technologies, Soochow University, Suzhou, Jiangsu, 215123, P. R. China

 † Electronic supplementary information (ESI) available: <sup>1</sup>H and <sup>13</sup>C-NMR spectra, HRMS, EA and HPLC of all target compounds; supplementary computational, photophysical device data. See DOI: <https://doi.org/10.1039/d3cc05761e>

 ‡ The research data supporting this publication can be accessed at <https://doi.org/10.17630/87972673-41de-4d34-9fd1-cfd23e633741>

§ Equal contribution.





Fig. 1 Chemical structures, photophysical properties and device properties of **DDiKta** and **DDiKta-F**.

3-bis(carbazolyl)benzene (mCP). The device with **DDiKta-F** showed an  $\text{EQE}_{\text{max}}$  of 15.3% emitting at a  $\lambda_{\text{EL}}$  of 493 nm (FWHM of 46 nm) with an improved efficiency roll-off at 100  $\text{cd m}^{-2}$  of 35% compared to the devices with **DDiKta** (56%)<sup>15</sup> and **DikTa** (44%) (Fig. 1).<sup>11</sup>

Theoretical calculations were out to investigate the effect of the incorporation of the fluorene bridge on the optoelectrical properties of the emitter compared to those of the reference, **DikTa**. The geometry in the ground state was first optimized using density functional theory at the PBE0/6-31G(d,p) level. The frontier molecular orbitals (FMOs) are delocalized over the entire  $\pi$ -conjugated system, and the HOMO and LUMO show an alternating distribution pattern similar to that of **DDiKta**, which is emblematic of MR-TADF compounds.<sup>15</sup> The calculated HOMO and LUMO levels of **DDiKta-F** are  $-5.94$  and  $-2.32$  eV, respectively. The HOMO–LUMO gap of 3.62 eV for **DDiKta-F** is smaller than that of **DDiKta** ( $\Delta E_{\text{HOMO-LUMO}} = 3.70$  eV), reflecting an increased conjugation in the former. The locked structure of the molecule contributed to small geometric changes between the  $S_0$  and  $S_1$  states, as depicted in Fig. S15 (ESI<sup>†</sup>). Thus, it is expected that the emission spectrum will be narrow and that there will be a small Stokes shift. The emission spectra of both **DikTa** and **DDiKta-F** under vacuum were simulated using Frank–Condon analysis based on the  $S_1$ – $S_0$  transition at the TDA-DFT-PBE0/6-31G(d,p) level (Fig. S16, ESI<sup>†</sup>). The simulated spectrum of **DikTa** shows an emission band peaking at  $\lambda_{\text{PL}} = 428$  nm and a small FWHM = 14 nm, which closely aligns with the emission in hexane at  $\lambda_{\text{PL}} = 436$  nm (FWHM = 21 nm). By contrast, the simulated emission spectrum of **DDiKta-F** is red-shifted at  $\lambda_{\text{PL}} = 474$  nm and is slightly broader (FWHM = 18 nm). We previously demonstrated that DFT calculations do not accurately predict the excited-state properties of MR-TADF emitters.<sup>16</sup> Here, we employed SCS-ADC(2)/cc-pVDZ calculations to accurately model the excited states of **DDiKta-F**.<sup>16</sup> Difference density plots provide information on the changes in the electron density distribution in the excited states compared to that of the ground state. The difference density plots between  $S_0$  and each of the  $S_1$  and  $T_1$  states, calculated for the  $S_0$  optimized geometry, reveal that these excited states have SRCT characteristics typical of MR-TADF emitters. The calculated energies of the  $S_1$  and  $T_1$  states are 3.34 and 3.08 eV, respectively, which are lower than those of **DikTa** ( $S_1/T_1 = 3.45/3.18$  eV) and **DDiKta** ( $S_1/T_1 = 3.39/3.12$  eV), indicating that the emission in this compound should be red-shifted compared



Fig. 2 (a) Distribution of FMOs of **DDiKta-F**, calculated at the PBE0/6-31G(d,p) level. (b) Difference density plots of  $S_1/S_2$  and  $T_1/T_2$  excited states, calculated at the SCS-ADC(2)/cc-pVDZ level for **DDiKta-F**, where  $f$  is the oscillator strength. The dashed lines in each figure reference the calculated values of **DikTa** at the same level of theory.<sup>17</sup>

to the two reference emitters. The calculated  $\Delta E_{\text{ST}}$  for **DDiKta-F** is 0.26 eV, which is similar to those of **DikTa** (0.26 eV)<sup>17</sup> and **DDiKta** (0.27 eV) (Fig. 2).<sup>15</sup>

The calculated spin–orbit coupling matrix element (SOCME) value between  $S_1$  and  $T_1$  is  $0.37 \text{ cm}^{-1}$  based on the  $T_1$ -optimized geometry, while the SOCME values between  $S_1$  and the four closely lying higher triplet excited states range from 0.07 to  $5.93 \text{ cm}^{-1}$ . In particular, the large  $\langle S_1 | \hat{H}_{\text{SOC}} | T_3 \rangle$  value of  $5.93 \text{ cm}^{-1}$  is attributed to an  $n$ - $\pi^*$  transition localized on the carbonyl groups (Fig. S18, ESI<sup>†</sup>).<sup>17</sup> These closely lying intermediate triplet states can participate in the RISC mechanism between  $T_1$  and  $S_1$  mediated by spin-vibronic coupling.<sup>18</sup>

The electrochemical properties of **DDiKta-F** and **DikTa** were investigated using cyclic voltammetry (CV) and differential pulse voltammetry (DPV) in deaerated DCM with 0.1 M tetra- $n$ -butylammonium hexafluorophosphate as the supporting electrolyte (Fig. S19, ESI<sup>†</sup>). The CV results show that the oxidation is irreversible while the reduction is a quasi-reversible process. The oxidation and reduction potentials,  $E_{\text{ox}}$  and  $E_{\text{red}}$ , determined, respectively, from the first oxidation and reduction peaks of the DPV, are 1.34 and  $-1.48$  V vs. SCE. The corresponding HOMO/LUMO levels and energy gap ( $\Delta E$ ) are  $-5.68/-2.86$  and 2.82 eV, respectively. The HOMO/LUMO are both destabilized compared to those of **DDiKta** ( $-5.97/-3.07$  eV)<sup>15</sup> and **DikTa** ( $-6.10/-2.99$  eV), implying that the fluorene bridge acts as an electron donor. As a result,  $\Delta E$  was smaller than those of **DDiKta** (2.90 eV) and **DikTa** (3.03 eV).

The absorption spectrum of the diluted toluene solution ( $10^{-5}$  M), shown in Fig. 3, exhibits two major bands. The band between 300 and 400 nm is linked to a  $\pi$ - $\pi^*$  transition delocalized over the whole skeleton, and the band at 375 nm is associated with the absorption of the central fluorene unit, both assigned from analysis of the TDA-DFT calculations (Fig. S17, ESI<sup>†</sup>). The lower energy band at 453 nm and shoulder at 431 nm are characteristics of an SRCT excited state transition for MR-TADF emitters (Fig. S17, ESI<sup>†</sup>). The SRCT band of **DDiKta-F** is red-shifted and more intense ( $\epsilon = 25 \times 10^3 \text{ M}^{-1} \text{ cm}^{-1}$ ) than those of **DDiKta** ( $\lambda_{\text{abs}} = 440$  nm and  $\epsilon = 10.4 \times 10^3 \text{ M}^{-1} \text{ cm}^{-1}$ ) and **DikTa** ( $\lambda_{\text{abs}} = 433$  nm and  $\epsilon = 21 \times 10^3 \text{ M}^{-1} \text{ cm}^{-1}$ ) due in part to its larger  $\pi$ -conjugation.<sup>15</sup> The photoluminescence (PL) spectrum of **DDiKta-F** in toluene, shown in





**Fig. 3** (a) Absorption and SS PL spectra obtained in toluene at RT. Inset: Photograph of **DDiKtA-F** in toluene and irradiated with a UV torch ( $\lambda_{\text{exc}} = 365$  nm). (b) SS PL and delayed emission spectra (1–10 ms), collected in 2-MeTHF at 77 K ( $\lambda_{\text{exc}} = 340$  nm).

Fig. 3a, has a peak maximum,  $\lambda_{\text{PL}}$ , of 476 nm, a shoulder at 511 nm, and an FWHM of 32 nm. The shoulder peak arises from the vibrational energy levels of the molecule, a typical characteristic of MR-TADF emitters.<sup>19,20</sup> This emission is red-shifted compared to those of **DDiKtA** ( $\lambda_{\text{PL}} = 470$  nm) and **DiKtA** ( $\lambda_{\text{PL}} = 453$  nm).<sup>15</sup> The emission of **DDiKtA-F** shows a modest positive solvatochromism (Fig. S20, ESI<sup>†</sup>), which is consistent with the emissive excited state of SRCT. The energies of the  $S_1$  and  $T_1$  states, determined from the onsets of the steady-state PL and phosphorescence spectra at 77 K in 2-MeTHF glass are 2.63 and 2.43 eV, respectively (Fig. 3b); thus,  $\Delta E_{\text{ST}} = 0.20$  eV. This value is similar in magnitude to those of **DiKtA** (0.22 eV in frozen toluene) and **DDiKtA** (0.21 eV in frozen toluene). The photoluminescence quantum yield,  $\Phi_{\text{PL}}$ , in toluene is 34%, which decreases to 31% upon exposure to air (Fig. S21, ESI<sup>†</sup>). No delayed emission was observed in toluene and the lifetime of the emission decay,  $\tau_{\text{PL}}$ , was 4.5 ns (Fig. S21, ESI<sup>†</sup>), which is similar to that of **DiKtA** ( $\tau_{\text{PL}} = 5.1$  ns).<sup>11</sup>

With a view to employ **DDiKtA-F** as an emitter in OLEDs and to cross-compare their device performance with those of **DDiKtA** and **DiKtA**, we next investigated the photophysical properties of this emitter as doped films in mCP. The 2 wt% doped film of **DDiKtA-F** in mCP emits at 494 nm with a FWHM of 49 nm (Fig. 4a), an emission that is red-shifted compared to those of **DDiKtA** ( $\lambda_{\text{PL}} = 491$  nm) and **DiKtA** ( $\lambda_{\text{PL}} = 467$  nm) in 2 wt% doped films in mCP.<sup>17</sup> We identified that 2 wt% doping provided the highest  $\Phi_{\text{PL}}$  of 78%, while the  $\Phi_{\text{PL}}$  decreased to 43% and the PL spectrum showed a pronounced red-shift from 491 to 507 nm when the doping concentration increased from 1 wt% to 10 wt% (Fig. S22, ESI<sup>†</sup>), implying that aggregation becomes an issue at this higher doping concentration. The  $\Phi_{\text{PL}}$  of the 2 wt% doped film in mCP decreased to 65% in air. The  $\Phi_{\text{PL}}$  of **DDiKtA-F** is slightly higher than those of both **DiKtA** ( $\Phi_{\text{PL}} = 46\%$ ) and **DDiKtA** ( $\Phi_{\text{PL}} = 65\%$ ) in 2 wt% doped films in mCP. At the same doping concentration, the  $\Phi_{\text{PL}}$  in the phosphine oxide-based hosts DPEPO and PPT are similar at 74 and 61% but the  $\lambda_{\text{PL}}$  are red-shifted at 510 and 511 nm, respectively, due to their higher polarity (Fig. S23, ESI<sup>†</sup>). The  $S_1/T_1$  energies, determined from the onsets of the steady-state PL and delayed emission spectra at 77 K in the 2 wt% doped films in mCP, are 2.58/2.40 eV, resulting in a  $\Delta E_{\text{ST}}$  of 0.18 eV (Fig. S26, ESI<sup>†</sup>), which

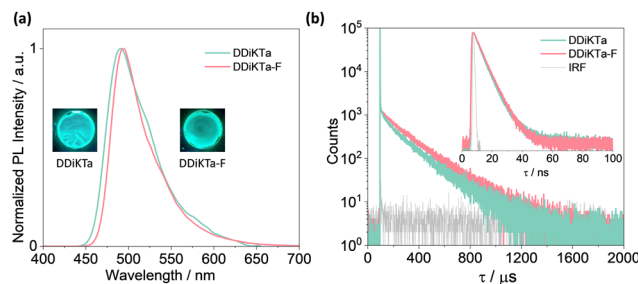


**Fig. 4** (a) SS PL spectra ( $\lambda_{\text{exc}} = 340$  nm); (b) time-resolved PL decays of **DDiKtA** and **DDiKtA-F** measured using MCS (inset: TRPL decays of the prompt component measured using TCSPC);  $\lambda_{\text{exc}} = 375$  nm.

is similar to that measured for 2-MeTHF glass. Temperature-dependent transient PL decay analysis reveals the expected increase in the delayed emission with increasing temperature, which confirms the TADF in the 2 wt% doped film in mCP (Fig. S24, ESI<sup>†</sup>). The emission decays with the associated average prompt ( $\tau_{\text{p}}$ ) and delayed ( $\tau_{\text{d}}$ ) lifetimes are 5.6 ns and 188  $\mu\text{s}$  (Table 1), respectively. These values are intermediate to those of **DDiKtA** ( $\tau_{\text{p}} = 5.9$  ns and  $\tau_{\text{d}} = 159$   $\mu\text{s}$ ) and **DiKtA** ( $\tau_{\text{p}} = 4.8$  ns and  $\tau_{\text{d}} = 242$   $\mu\text{s}$ ); in air, the delayed emission of **DDiKtA-F** was not completely quenched (Fig. S25, ESI<sup>†</sup>). From these photophysical measurements, the RISC rate constant ( $k_{\text{RISC}}$ ) of **DDiKtA-F** was determined to be  $2.16 \times 10^4 \text{ s}^{-1}$  (Table S2, ESI<sup>†</sup>),<sup>21,22</sup> which is intermediate to those of **DDiKtA** ( $k_{\text{RISC}} = 1.77 \times 10^4 \text{ s}^{-1}$ ) and **DiKtA** ( $k_{\text{RISC}} = 2.52 \times 10^4 \text{ s}^{-1}$ ).

Having identified the potential of **DDiKtA-F** as an emitter for OLEDs, we next fabricated vacuum-deposited devices. The devices have the following architecture: ITO/TAPC (35 nm)/TCTA (10 nm)/CzSi (10 nm)/x wt% emitter/mCP (20 nm)/TmPyPB (40 nm)/LiF (1 nm)/Al (100 nm), where indium tin oxide (ITO) is the anode and 4,4'-cyclohexylidenebis[N,N-bis(4-methylphenyl)benzamine] (TAPC) acts as the hole-transport layer. 9-(4-*tert*-butylphenyl)-3,6-bis(triphenylsilyl)-9H-carbazole (CzSi) is the exciton blocking layer, 1,3,5-tri(*m*-pyridin-3-ylphenyl)benzene (TmPyPB) acts as the electron-transporting material, and LiF modifies the work function of the aluminium cathode. The chemical structures of the materials used in these devices are shown in Fig. S27 (ESI<sup>†</sup>). The device stacks and their related performance are shown in Fig. 5 and Fig. S28 and S29 (ESI<sup>†</sup>), respectively.

The electroluminescence peak of the OLED,  $\lambda_{\text{EL}}$  of 493 nm and FWHM of 46 nm match those of the PL spectrum of the 2 wt% films in mCP ( $\lambda_{\text{PL}} = 494$  nm and FWHM = 49 nm). The EL is narrower compared to the previously reported device with

**Table 1** Photophysical data of **DDiKtA-F** and **DDiKtA** in 2 wt% doped films in mCP

Emitter	$\Phi_{\text{PL}}^a$ /%	$\lambda_{\text{PL}}/ \text{nm}$	FWHM/nm	$S_1^b/T_1^c$ /eV	$\Delta E_{\text{ST}}/ \text{eV}$	$\tau_{\text{p}}, \tau_{\text{d}}/ \text{ns}, \mu\text{s}$
<b>DDiKtA-F</b>	78	494	49	2.58, 2.40	0.18	5.6, 188
<b>DDiKtA</b>	68	491	60	2.64, 2.45	0.19	5.9, 159
<b>DiKtA</b> <sup>17</sup>	46	467	46	2.75, 2.55	0.20 <sup>11</sup>	4.8, 242

<sup>a</sup>  $\Phi_{\text{PL}}$  was measured using an integrating sphere under nitrogen ( $\lambda_{\text{exc}} = 340$  nm). <sup>b</sup> Obtained from the onset of the SS PL spectrum at 77 K. <sup>c</sup> Obtained from the onset of the delayed emission spectrum (1–10 ms) at 77 K ( $\lambda_{\text{exc}} = 340$  nm).





Fig. 5 (a) Device configuration and energy levels for each layer; (b) electroluminescence spectra for devices; (c)  $J$ - $V$ - $L$  characteristics; and (d) EQE and CE versus luminance characteristics.

**DDiKta** (9 wt% in DPEPO), which emitted at a  $\lambda_{\text{EL}}$  of 500 nm and had an FWHM of 59 nm.<sup>15</sup> This small red-shifted emission compared to the SS PL in 2 wt% mCP film can be attributed to a combination of the use of the higher polarity DPEPO host and higher doping concentrations. By contrast, the EL is red-shifted compared to the device with **DiKta** (3.5 wt% in mCP), which emitted at a  $\lambda_{\text{EL}}$  of 465 nm and had a FWHM of 59 nm.<sup>11</sup> The corresponding Commission Internationale de l'Éclairage (CIE) coordinates are (0.16, 0.50) for the device with **DDiKta-F**, which are close to those of the device with **DDiKta** (0.18, 0.53), yet are red-shifted compared to the device with **DiKta** (0.14, 0.18). The device with **DDiKta-F** exhibited an  $\text{EQE}_{\text{max}}$  of 15.3%, which is similar to those of **DDiKta** (19.0%) and **DiKta** (14.7%). Gratifyingly, the efficiency roll-off was less severe, with an EQE of  $100 \text{ cd m}^{-2}$  at 9.9% for the device with **DDiKta-F**, which was higher than those of **DDiKta** ( $\text{EQE}_{100} = 8.1\%$ ) and **DiKta** ( $\text{EQE}_{100} = 8.3\%$ ). This modestly improved efficiency roll-off can be explained by a higher figure of merit (FOM) that describes productive exciton utilization,  $\text{FOM} = \frac{k_{\text{r}}k_{\text{RISC}}}{k_{\text{ISC}}}$ ,<sup>23</sup> of  $4.75 \times 10^3 \text{ s}^{-1}$  for **DDiKta-F**, compared to those of  $4.71 \times 10^3$  and  $1.87 \times 10^3 \text{ s}^{-1}$  for **DDiKta** and **DiKta**, respectively.

In conclusion, we demonstrated an easy-to-access synthetic route for constructing a p-extended dimeric MR-TADF emitter by fusing two **DiKta** units onto a fluorene bridge. Through this strategy, the structural motion was reduced compared to that of the parent dimeric emitter **DDiKta**. This led to an improved  $\Phi_{\text{PL}}$  of 79% and a red-shifted and narrower emission at 494 nm (FWHM = 49 nm) in 2 wt% doped films in mCP. Moreover, the  $\Delta E_{\text{ST}}$  decreased to 0.18 eV, which led to a modest improvement in  $k_{\text{RISC}}$  from  $1.77 \times 10^4 \text{ s}^{-1}$  to  $2.16 \times 10^4 \text{ s}^{-1}$ . The device with **DDiKta-F** exhibited an  $\text{EQE}_{\text{max}}$  of 15.3% and emission at 493 nm. Owing to the faster  $k_{\text{RISC}}$ , the device exhibited a smaller efficiency roll-off of 35% at  $100 \text{ cd m}^{-2}$  than the devices with **DDiKta** (56%) and **DiKta** (44%). This emitter design, annelating multiple MR-TADF cores about a central fluorene, provides

a simple method to maintain narrowband emission in MR-TADF compounds while simultaneously enhancing the  $\Phi_{\text{PL}}$  and  $k_{\text{RISC}}$ .

S. W. thanks the China Scholarship Council (201906250199) for support. D.S. acknowledges support from the Royal Academy of Engineering Enterprise Fellowship (EF2122-13106). E. Z.-C. thanks the Engineering and Physical Sciences Research Council (EP/W015137/1, EP/W007517) for support. X.-H. Z. acknowledges support from the National Natural Science Foundation of China (Grant No. 52130304, 51821002) and the Collaborative Innovation Center of Suzhou Nano Science & Technology.

## Conflicts of interest

There are no conflicts to declare.

## References

- 1 C. W. Tang and S. A. VanSlyke, *Appl. Phys. Lett.*, 1987, **51**, 913.
- 2 M. A. Baldo, D. F. O'Brien, Y. You, A. Shoustikov, S. Sibley, M. E. Thompson and S. R. Forrester, *Nature*, 1998, **395**, 151–154.
- 3 A. Endo, K. Sato, K. Yoshimura, T. Kai, A. Kawada, H. Miyazaki and C. Adachi, *Appl. Phys. Lett.*, 2011, **98**, 083302.
- 4 Y. Tao, K. Yuan, T. Chen, P. Xu, H. Li, R. Chen, C. Zheng, L. Zhang and W. Huang, *Adv. Mater.*, 2014, **26**, 7931–7958.
- 5 H. Uoyama, K. Goushi, K. Shizu, H. Nomura and C. Adachi, *Nature*, 2012, **492**, 234–238.
- 6 Y. J. Cho, S. K. Jeon, S.-S. Lee, E. Yu and J. Y. Lee, *Chem. Mater.*, 2016, **28**, 5400–5405.
- 7 A. C. Arsenault, D. P. Puzzo, I. Manners and G. A. Ozin, *Nat. Photonics*, 2007, **1**, 468–472.
- 8 T. Hatakeyama, K. Shiren, K. Nakajima, S. Nomura, S. Nakatsuka, K. Kinoshita, J. Ni, Y. Ono and T. Ikuta, *Adv. Mater.*, 2016, **28**, 2777–2781.
- 9 H. Jiang, J. Jin and W. Y. Wong, *Adv. Funct. Mater.*, 2023, **33**, 2306880.
- 10 R. K. Konidena and K. R. Naveen, *Adv. Photonics Res.*, 2022, **3**, 2200201.
- 11 D. Hall, S. M. Suresh, P. L. dos Santos, E. Duda, S. Bagnich, A. Pershin, P. Rajamalli, D. B. Cordes, A. M. Z. Slawin, D. Beljonne, A. Köhler, I. D. W. Samuel, Y. Olivier and E. Zysman-Colman, *Adv. Opt. Mater.*, 2020, **8**, 1901627.
- 12 X. Li, Y.-Z. Shi, K. Wang, M. Zhang, C.-J. Zheng, D.-M. Sun, G.-L. Dai, X.-C. Fan, D.-Q. Wang, W. Liu, Y.-Q. Li, J. Yu, X.-M. Ou, C. Adachi and X.-H. Zhang, *ACS Appl. Mater. Interfaces*, 2019, **11**, 13472–13480.
- 13 Y. Yuan, X. Tang, X.-Y. Du, Y. Hu, Y.-J. Yu, Z.-Q. Jiang, L.-S. Liao and S.-T. Lee, *Adv. Opt. Mater.*, 2019, **7**, 1801536.
- 14 C. Zhou, A. Shatskiy, A. Z. Temerdashev, M. D. Kärkäs and P. Dinér, *Commun. Chem.*, 2022, **5**, 92.
- 15 D. Sun, S. M. Suresh, D. Hall, M. Zhang, C. Si, D. B. Cordes, A. M. Z. Slawin, Y. Olivier, X. Zhang and E. Zysman-Colman, *Mater. Chem. Front.*, 2020, **4**, 2018–2022.
- 16 D. Hall, J. C. Sancho-García, A. Pershin, G. Ricci, D. Beljonne, E. Zysman-Colman and Y. Olivier, *J. Chem. Theory Comput.*, 2022, **18**, 4903–4918.
- 17 S. Wu, L. Zhang, J. Wang, A. Kumar Gupta, I. D. W. Samuel and E. Zysman-Colman, *Angew. Chem., Int. Ed.*, 2023, **62**, e202305182.
- 18 T. J. Penfold, E. Gindensperger, C. Daniel and C. M. Marian, *Chem. Rev.*, 2018, **118**, 6975–7025.
- 19 Y. Kondo, K. Yoshiura, S. Kitera, H. Nishi, S. Oda, H. Gotoh, Y. Sasada, M. Yanai and T. Hatakeyama, *Nat. Photon.*, 2019, **13**, 678.
- 20 X. Qiu, G. Tian, C. Lin, Y. Pan, X. Ye, B. Wang, D. Ma, D. Hu, Y. Luo and Y. Ma, *Adv. Opt. Mater.*, 2020, **9**, 20200.
- 21 K. Masui, H. Nakanotani and C. Adachi, *Org. Electron.*, 2013, **14**, 2721–2726.
- 22 Y. Tsuchiya, S. Diesing, F. Bencheikh, Y. Wada, P. L. dos Santos, H. Kaji, E. Zysman-Colman, I. D. W. Samuel and C. Adachi, *J. Phys. Chem. A*, 2021, **125**, 8074–8089.
- 23 S. Diesing, L. Zhang, E. Zysman-Colman and I. Samuel, *ChemRxiv*, 2023, preprint, DOI: [10.26434/chemrxiv-2023-c0hgg](https://doi.org/10.26434/chemrxiv-2023-c0hgg).

